RSC Advances

ROYAL SOCIETY OF CHEMISTRY

www.rsc.org/advances

RSC Advances

ARTICLE

Polypyrrole-assisted synthesis of roselike MoS_2/nitrogen-containing carbon/graphene hybrids and their robust lithium storage performances

Received 00th January 20xx,
Accepted 00th January 20xx

DOI: 10.1039/x0xx00000x

www.rsc.org/

Zhiyan Guo,* Yang Zhong, Zongwei Xuan, Changming Mao, Fanglin Du and Guicun Li*

Roselike MoS_2/nitrogen-containing carbon/graphene (MoS_2/NC/G) hybrids have been successfully synthesized via a facile polypyrrole (PPy)-assisted hydrothermal approach in combination with high-temperature calcination. The obtained MoS_2/NC/G hybrids manifest roselike MoS_2 composed of nanosheets coupled uniformly on NC/G nanosheets due to the strong interaction between MoS_2 and the abundant nitrogen-containing functional groups of NC. When used as an anode materials for lithium ion batteries, the MoS_2/NC/G hybrids exhibit enhanced electrochemical energy storage performances compared to the bare MoS_2 nanosheets, including high specific capacity (1570.6 mAh g^{-1} at 0.1 A g^{-1}), excellent rate capability (704.8 mAh g^{-1} at 5 A g^{-1}) and good cycling stability (96.4% capacity retention after 100 cycles at 0.2 A g^{-1}). The enhanced lithium storage properties of the MoS_2/NC/G hybrids can be ascribed to the boosted electronic conductivity arising from the novel hybrids nanostructures of MoS_2/NC/G.

Introduction

Rechargeable lithium-ion batteries (LIBs) have been regarded as one of the most promising power technology in the applications of energy storage stations, electric vehicles and so on.[1,2] High energy and power density, excellent security, long cycling performance is a key technology for the development of LIBs.[3] Nowadays, commercially used carbon-based anode materials are limited by their intrinsically low theoretical capacity value of 372 mAh g^{-1}.[4] Molybdenum disulfide (MoS_2), a layered transition metal dichalcogenide, in which S–Mo–S layers are held together by weak van der Waals forces, is regarded as a promising anode materials in LIBs because of high theoretical specific capacity (*ca.* 670 mAh g^{-1}).[5] However, the rate capability and cyclic stability of MoS_2 become poor in the subsequent cycles owing to the low conductivity and poor cyclability of Li_2S.[6] Moreover, the pulverization and aggregation of MoS_2 during the discharge-charge cycle resulting from a significant volume change can lead to fast capacity fading.[7]

A variety of methods have been employed to address the above issues. Previous reports mostly focus on size and morphology control of MoS_2,[8] or construction of composite materials of MoS_2 and conductive carbonaceous materials, such as carbon nanotubes,[9] carbon nanofibers[6] or graphene[7,10–12]. For examples, Wang *et al.*[8] have reported a simple method for the synthesis of 3D tubular architectures constructed by single-layered MoS_2 via a mixed solution reaction, and exhibited greatly improved Li^+ storage properties. Lou *et al.*[9] have reported a simple glucose-assisted hydrothermal method to directly grow MoS_2 nanosheets on the CNT backbone, which shown greatly enhanced lithium storage properties compared with the pure MoS_2. Graphene, a single layer of sp^2 carbon atoms, has attracted tremendous interest owning to its novel geometrical structure and excellent electrical conductivity.[13] Meanwhile, it is an ideal substrate for growth and anchoring nanomaterials, such as metal, metal oxide, metal sulfide nanoparticles, functionally as catalysts for hydrogen evolution reaction,[14] lithium storage,[15] capacitance,[16] Raman enhancement[17] and so on. MoS_2/graphene nanocomposites have already been successfully applied as anode materials for LIBs[7, 10-12]. Nevertheless, owing to the general incompatibility between graphene and inorganic nanoparticles, the growth of inorganic nanoparticles with uniform morphology and controllable sizes on a graphene substrate is difficult technically.

Recently, nitrogen-containing carbon (NC) has received considerable interest because nitrogen-containing functional groups can not only provide more active sites for lithium storage, but also be used for the conjugation of metallic ions to help the growth of MoS_2 on the surface of graphene.[18-20] Polypyrrole (PPy) is one of the most promising conducting polymers, which facilitates the incorporation of nitrogen-containing functional groups into carbon matrix. In addition, the pyrrole monomers can be easily polymerized on both surfaces of graphene oxide (GO) due to the π-π stacking between PPy and GO layers,[21,22] which inspires us to find a new route to fabricate hybrids nanostructure in which MoS_2 could grow uniformly on the surfaces of PPy/GO. Herein, we report an efficient strategy for the synthesis of MoS_2/NC/G hybrids by a facile PPy-

Address here.
Address here.
Address here.
† Footnotes relating to the title and/or authors should appear here.
Electronic Supplementary Information (ESI) available: [details of any supplementary information available should be included here]. See DOI: 10.1039/x0xx00000x

assisted hydrothermal approach in combination with high-temperature calcination, which exhibit excellent lithium storage performances including high specific capacity, excellent rate capability and good cycling stability.

Experimental

Synthesis of GO

Graphene oxide (GO) was synthesized from natural graphite flakes by a modified Hummer method.[23]

Synthesis of PPy/GO composite

Pyrrole (4 mL) and GO (200 mg) at the weight ratio of 10:1 were dispersed in 900 mL of 0.1 mol L^{-1} HCl aqueous solution by ultrasonication for 20 min. Then 100 mL of HCl (0.1 mol L^{-1}) aqueous solution containing ammonium peroxydisulfate (13.6 g) was rapidly added to the above mixture suspension solution at 0–5°C. The polymerization reaction was carried out for 12 h without any disturbance. Then the black precipitate was filtered off, washed with ammonium hydroxide, deionized water, and ethanol several times, and then dried at 80 °C for 24 h.

Synthesis of MoS_2/NC/G hybrids

The obtained PPy/GO composite (ca. 120 mg) were redispered into 60 mL H_2O with assistance of ultrasonication about 30 min. Then 0.8 g sodium molybdate ($Na_2MoO_4.2H_2O$) and 1. 0 g thiourea were added to the PPy/GO suspension by ultrasonication for another 30 min. The mixture was transfered a Teflon-lined autoclave and kept at 200 °C for 20 h. After cooling down to room temperature, the black precipitate was collected by centrifugation, washed with ethanol and water for several times, and dried at 80 °C for 24 h. Afterwards, the MoS_2/PPy/GO products were further annealed at 800 °C for 2 h under the atmosphere of 5% H_2, balanced by Ar for 2 h with a heating rate of 3 °C min^{-1}.The preparation of the bare MoS_2 nanosheets is similar to the one for MoS_2/NC/G hybrids except the addition of PPy/GO.

Characterization

The crystalline structures of the samples were characterized by X-ray powder diffraction (XRD Rigaku D-max-γA XRD with Cu K_α radiation, λ = 1.54178 Å) from 5° to 90°. SEM images were measured by Field-emission scanning electron microscopy (FE-SEM, JSM-6700F from JEOL) and TEM images were measured by a transmission electron microscopy (TEM, FEI Tecnai G20). Thermogravimetric (TG) analyses were performed on a TG instrument (NETZSCH STA 449C) using a heating rate of 10 °C min^{-1} in air from 30 °C to 700 °C. The X-ray photoelectron spectroscopy (XPS) analysis was performed on a Perkin-Elmer PHI 550 spectrometer with Al Kα (1486.6 eV) as the X-ray source. XPS spectra were taken after all binding energies were referenced to the C 1s neutral carbon peak at 284.8 eV, and the elemental compositions were determined from peak area ratios after correction for the sensitivity factor for each element.

Electrochemical test

The electrochemical measurements were carried out using CR2032-type coin cell at room temperature. The working electrodes were fabricated by mixing the active materials, carbon black (Super-P), and poly(vinyl difluoride) (PVDF) at a weight ratio of 70:20:10 and the mixture was mixed with N-methyl pyrrolidone (NMP) to form slurry and then pasted onto pure Cu foil. The electrode area was 1.54 cm^2. Pure lithium foil was used as the counter electrode and separated by a Celgard 2500 membrane separator. A solution of 1 mol L^{-1} $LiPF_6$ in ethylene carbonate/dimethyl carbonate (1:1 by volume) was used as the electrolyte. The cells were assembled in a glove box filled with high purity argon gas and soaked overnight before test. The galvanostatic discharge-charge experiments were performed over a voltage range of 0.01–3.0 V (vs. Li^+/Li) at different current density using a LAND CT2001A battery tester. Electrochemical impedance spectroscopy (EIS) measurements were carried out on an Autolab PGSTAT302N electrochemical workstation by applying a sine wave with the amplitude of 10.0 mV over the frequency range from 100 kHz to 10 mHz. Cyclic voltammetry (CV) curves were performed using the same workstation as EIS measurements at a scanning rate of 0.1 mV s^{-1}.

Results and discussion

The synthetic procedure of the MoS_2/PPy/GO hybrids is illustrated in Fig. 1. To improve the compatibility between GO (Fig. S1 a) and MoS_2, PPy was first coated uniformly on both surfaces of GO by in-situ polymerization of pyrrole. As shown in Fig. 1b, the thickness and lateral dimension of the PPy/GO composite nanosheets (Fig. S1 b) are 20–25 nm and 1–2 μm, respectively. After hydrothermal growth of MoS_2, it is found that roselike MoS_2 composed of nanosheets were coupled on the PPy/GO composite nanosheets due to the strong interaction between MoS_2 and PPy (Fig. 1c). The MoS_2/PPy/GO hybrids can be converted into MoS_2/NC/G hybrids by high temperature calcination.

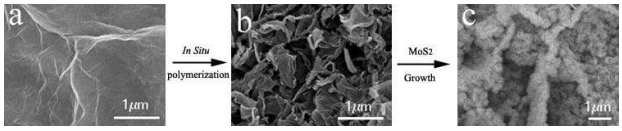

Fig. 1 The overall synthetic procedure of MoS_2/PPy/GO hybrids. The corresponding SEM images of GO (a), PPy/GO (b), MoS_2/PPy/G (c).

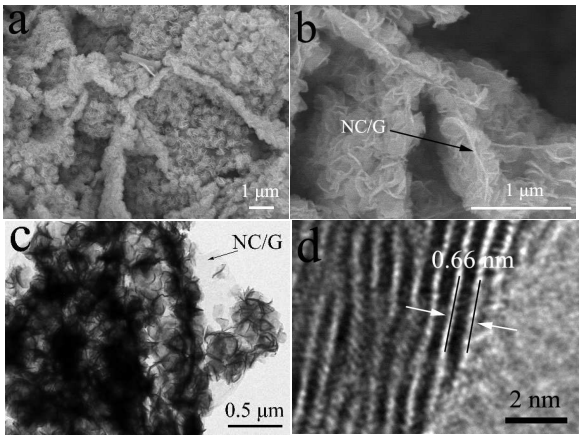

Fig. 2 SEM images of the MoS_2/NC/G hybrids (a,b), TEM image of a single MoS_2/NC/G hybrids (c), and High resolution TEM image of MoS_2 nanosheets (d).

Fig. 2 a and b show typical SEM images of the MoS_2/NC/G hybrids. Low-magnification SEM image (Fig. 2 a) reveals that the product has a two-dimensional structure and the surface is covered with roselike MoS_2 subunits. As shown in high-magnification SEM image (Fig. 2b), it is clear that the PPy/GO composite nanosheets are converted into NC/G composite nanosheets as indicated by an arrow due to the carbonization and thermal reduction process. Moreover, the roselike MoS_2 subunits comprising of thin nanosheets are

coupled strongly on the surfaces of NC/G composite nanosheets, which is similar to that of the MoS_2/PPy/GO hybrids, indicating that the MoS_2/NC/G hybrids possess high thermal stability. Compared with the MoS_2/NC/G hybrids, bare MoS_2 tends to form microspheres composed of nanosheets (Fig. S2 a and b). The roselike MoS_2 subunits closely attached on the surfaces of the NC/G nanosheets can be further confirmed by TEM observation (Fig. 2 c). In addition, the NC/G nanosheets can be also found in the TEM image as described by an arrow. Typical HRTEM image of the MoS_2/NC/G hybrids is represented in Fig. 2d. The observed fringes correspond to the interplanar distance of 0.66 nm, which are in good agreement with the lattice spacing of the (002) planes of the bare MoS_2 nanosheets (Fig. S2 c).[24] Meanwhile, the fringes with interplanar spacing of 2.09 Å corresponding to (200) facet of the Mo_2N based on a face-centered cubic crystal structure be clearly observed in the HRTEM image (Fig. S2 d).[25] Intriguing transition metal nitrides have superior properties in some respects such as high conductivity,[26] which are desired for LIBs.

The crystallographic structure and phase purity of annealed MoS_2/NC/G hybrids are measured by XRD analysis (Fig. S3). The XRD pattern of the products in the first step can be well indexed to hexagonal MoS_2, in good agreement with the standard data (JCPDS card no.37-1492; space group P63/mmc; a = 3.161 Å, c = 12.299 Å). Besides the XRD peaks of hexagonal MoS_2, the XRD patterns of the products in the second step show another peak, which can be well matched with a strong peak (111) and (200) of cubic Mo_2N (JCPDS card no.25-1366), which may be caused by slow nitridation under the circumstance of PPy pyrolysis.

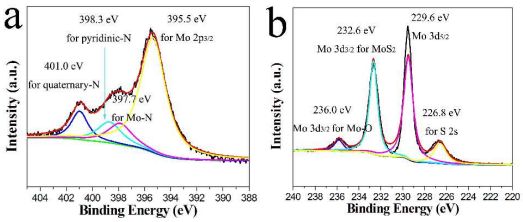

Fig. 3 Typical high-resolution XPS spectra of N 1s and Mo 2p (a), Mo 3d and S 2s (b) for the MoS_2/NC/G hybrids.

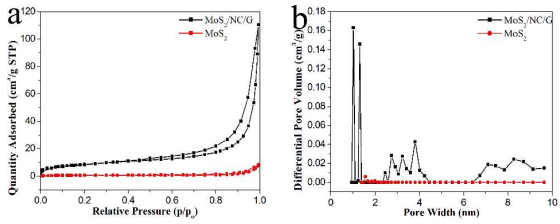

Fig. 4 N_2 adsorption-desorption isotherms (a) and pore size distribution (b) of the MoS_2/NC/G hybrids and the bare MoS_2 nanosheets.

XPS measurement was applied to analyze the chemical states of the elements in MoS_2/NC/G hybrids and the bare MoS_2 nanosheets. It can be clearly seen that a peak corresponding to N1s appears at around 399 eV, suggesting the presence of N in the hybrids (Fig. S4). There is no peak related to N and C species detected from the the bare MoS_2 nanosheets. The surface elemental compositions from XPS analysis shows that 3.7 at.% N are contained in MoS_2/NC/G hybrids. XPS N1s spectrum of the MoS_2/NC/G hybrids is displayed in Fig. 3 a, and fitted by three components of binding energies of about 401.0, 398.3, and 397.7 eV. The peaks at 398.3 and 401.0 eV are assigned to pyridinic N and quaternary N, respectively.[27] The peak at around 397.7 eV can be assigned to N 1s which is characteristic for a metal nitride material,[28] which is in agreement with XRD and HRTEM results. The presence of nitrogen at the carbon surface enhance the reactivity and electric conductivity according to previous reports.[29,30] Peaks located at 229.6 and 232.6 eV can be attributed to Mo $3d_{5/2}$ and $3d_{3/2}$, respectively. The adsorption-desorption isotherm of MoS_2/NC/G hybrids exhibits a type IV adsorption branch with a H3 hysteresis loop, which is characteristic of the mesoporous structure (Fig. 4a). The corresponding Brunauer–Emmett–Teller (BET) surface area are calculated to be 30.43 m^2 g^{-1}, which are much higher than those of the bare MoS_2 nanosheets about 2.35 m^2 g^{-1}. The pore size distributions of the MoS_2/NC/G hybrids are shown in Fig. 4b. The pore size distributions tend to concentrate on 0.5–1.5 nm and 2.5–10 nm, revealing the presence of meso- and micro-pores in the NC/G nanosheets. However, the bare MoS_2 nanosheets exhibit much less pores than the MoS_2/NC/G hybrids. The porous structures of the MoS_2/NC/G hybrids would offer more favorable route for lithium ion diffusion, which will benefit the electrochemical lithium storage performances. TG analysis was employed to determine the content of MoS_2 present in MoS_2/NC/G hybrids. The MoS_2/NC/G hybrids underwent significant weight loss mainly below 500 °C (Figure S5 b), which can perhaps be attributed to combustion of NC and graphene, and oxidation of MoS_2 to MoO_3.[9] We confirmed that the remaining product after the TG measurement is MoO_3 (XRD pattern in Fig. S6), which has a weight fraction of about 79%, estimate that the MoS_2 content in the MoS_2/NC/G hybrids is approximately 87%.

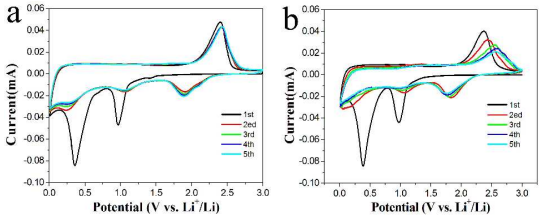

Fig. 5 CV curves of the MoS_2/NC/G hybrids (a), and the bare MoS_2 nanosheets (b) measured in the voltage range of 0.01–3.0 V with a scan rate of 0.1 mV s^{-1}.

CV measurements were performed to investigate the phase transformation and ionic diffusion process of the MoS_2/NC/G hybrids and the bare MoS_2 nanosheets during the electrode reaction process. In the first cathodic scan (Fig. 5a), the 0.96 V peak is assigned to the Li^+ intercalation into MoS_2 layers for forming Li_xMoS_2, 0.36 V peak is attributed to the complete reduction of MoS_2 to Mo and Li_2S. These peaks disappears completely in the subsequent processes. Instead, new peaks at 1.90, 1.06, and 0.25 V emerge, which perhaps are attributed to a multi-step Li^+ insertion mechanism. In the anodic scans, the peaks around 2.42 V can be associated with the conversions of Li_2S to S.[31] It is crucial that the oxidation peak of the MoS_2/NC/G hybrids electrode at 2.42 V does not change in subsequent anodic sweeps, corresponding to the reversible decomposition of Li_2S, indicating the reversibility of the lithiation/delithiation process and the lowest internal diffusion resistance of the MoS_2/NC/G hybrids. As for the bare MoS_2

nanosheets, the CV profile (Fig. 5 b) in the first cycle is similar with that of the MoS_2/NC/G hybrids. However, higher potentials of oxidation peaks and lower potentials of corresponding reduced peaks compared to MoS_2/NC/G hybrids are observed, indicating the large polarization of the bare MoS_2 nanosheets during the charge and discharge process. The polarization is associated with the transfer delay of the electrons on the active material/electrolyte interface.[32,33] In contrast, the MoS_2/NC/G hybrids electrode facilitates electron and ion transfer during the electrochemical reaction process.

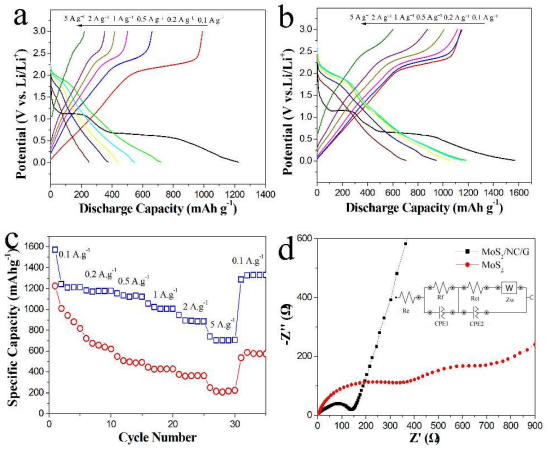

Fig. 6 Galvanostatic discharge-charge profiles of the bare MoS_2 nanosheets electrode (a) and the MoS_2/NC/G hybrids electrode (b) at various rates. Comparison of the rate performance of the MoS_2/NC/G hybrids electrode electrode and the bare MoS_2 nanosheets electrode (c). EIS spectra of the of the MoS_2/NC/G hybrids and the bare MoS_2 nanosheets cells after CV test (d). Equivalent circuits for the MoS_2/NC/G hybrids electrode (The inset in d).

The lithium storage performances of the MoS_2/NC/G hybrids and the bare MoS_2 nanosheets were further evaluated by galvanostatic charge-discharge cycling. As shown in Fig. 6a, the plateaus on the charge/discharge curves of MoS_2/NC/G hybrids and the bare MoS_2 nanosheets are in consistent with the conversion peaks on its CV curves (Fig. 5a and b). The initial discharge and charge capacities of the MoS_2/NC/G hybrids were found to be 1570.6 and 1143.7 $mAhg^{-1}$, respectively. Such a high initial lithium storage capacity might be associated with the hybrids nanostructure of MoS_2/NC/G. The irreversible capacity loss of approximately 27.2% can be mainly attributed to the formation of the solid-electrolyte interface (SEI). Rate performances of the MoS_2/NC/G hybrids and the bare MoS_2 nanosheets were examined at various current densities in the range of 0.1–5 A g^{-1} (Fig. 6c). Reversible capacities of around 1570.6, 1182.9, 1153.7, 1056.4, 947.0, and 704.8 mA h g^{-1} are achieved for the MoS_2/NC/G hybrids at 0.1, 0.2, 0.5, 1, 2, and 5 A g^{-1}, while the bare MoS_2 nanosheets deliver inferior capacities of 1226.5, 721.3, 548.3, 443.9, 375.5, and 248.6 mA h g^{-1} at 0.1, 1, 2, and 5 A g^{-1}, respectively. When the current rate reverses back to 0.1 A g^{-1}, the discharge capacities can recover to the original value immediately, indicating that the MoS_2/NC/G hybrids possess good cycling stability due to the high structure stability.

Kinetic differences of the MoS_2/NC/G hybrids and MoS_2 electrodes were investigated by EIS after CV test. As shown in Fig. 6d, the high-frequency semicircle corresponds to the solid SEI film resistance (R_f) and the constant phase element (CPE1), the semicircle in the medium-frequency region is assigned to the charge-transfer impedance (Rct) and the constant phase element of the electrode-electrolyte interface (CPE2), and W is associated with the Warburg impedance. Obviously, the SEI film resistance (Rf) and charge-transfer resistance (Rct) of the MoS_2/NC/G hybrids based on the modified equivalent circuit (the inset in Fig. 6d) are fitted to be 52.3 and 56.8 Ω, respectively, which are significantly lower than those of the bare MoS_2 nanosheets (119 and 614 Ω). The results confirm that the NC/G nanosheets have distinctively boosted the electronic conductivity of the MoS_2/NC/G hybrids and facilitate the efficient and fast transfer of electrons and Li^+ ions, leading to the high rate capability of the MoS_2/NC/G hybrids.

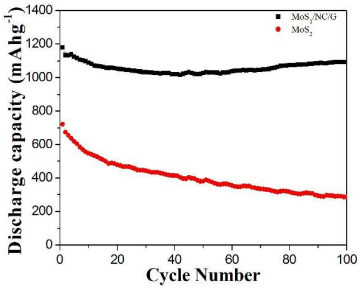

Fig. 7 Cycling performance of the MoS_2/NC/G hybrids and MoS_2 electrodes at 0.2 A g^{-1}.

Fig. 7 gives the long-term cycling performance of the MoS_2/NC/G hybrids and the bare MoS_2 electrodes at a current rate of 0.2 A g^{-1}. During the first 40 cycles, the discharge capacity stabilizes around 1021 mAh g^{-1} , and then gradually increases to 1093 mAh g^{-1} at the 100 th cycle (96.4% of the second cycle capacity). The increasing specific capacity with cycling is common for various nanostructured metal oxide/sulfide electrodes and could be attributed to the growth of the gel-like polymeric layer and possibly electrochemical activation of hybrids composites.[34,35] In contrast, the bare MoS_2 nanosheets delivers fast capacity fading, and a capacity of only around 285 $mAhg^{-1}$ was retained after 100 cycles (42.3% of the second cycle capacity). These results reveal the excellent electrochemical stability and cycling performance of the MoS_2/NC/G hybrids.

Conclusions

In conclusion, we have developed a facile PPy-assisted approach to successfully synthesize the MoS_2/NC/G hybrids in which roselike MoS_2 subunits composed of nanosheets are closely attached on the surfaces of the NC/G nanosheets. The presence of PPy can not only couple the MoS_2 with graphene oxide, but also be converted into NC to increase electronic conductivity of the hybrids. As a result, the MoS_2/NC/G hybrids exhibit improved lithium ion storage performances including higher specific capacity, superior rate performance, and good cycling stability in comparison with the bare MoS_2 nanosheets. This facile strategy can be extended to fabricate other hybrid electrode materials to couple two incompatible components which may serve as ideal candidates in catalysts, sensors, supercapacitors, as well as LIBs.

Acknowledgements

This work was supported by the National Natural Science Foundation of China (No. 51272113, No. 51272115), A Project of Shandong Province Higher Educational Science and Technology Program (J13LA10), A Project of Shandong Province Higher Educational Science and Technology Program (J14LA15), A Project of Shandong Province Higher Educational Science and Technology Program (J15LA12) and Natural Science Foundation of Shandong Province (No.ZR2012EMM001).

Notes and references

College of Materials Science and Engineering, Qingdao University of Science and Technology, Qingdao 266042, China.* Corresponding authors. Tel.: 86-532-84022814; fax: 86-532-84022814. E-mail: zhiyanguo@qust.edu.cn and guicunli@qust.edu.cn

†Electronic Supplementary Information (ESI) available: [SEM and TEM images, XRD patterns, XPS survey spectra, TG curve] See DOI: 10.1039/b000000x/

1 J. B. Goodenough and K Park, *J. Am. Chem. Soc.*, 2013, **135**, 1167.
2 J. M. Tarascon and M. Armand, *Nature*, 2001, **414**, 359.
3 B. Guo, X. Yu, X. Sun, M. Chi, Z. Qiao, J Liu, Y. Hu, X Yang, J. B. Goodenough and S. Dai, *Energy Environ. Sci.*, 2014,**7**, 2220.
4 M. V. Reddy, G. V. Subba Rao and B. V. R. Chowdari, *Chem. Rev.*, 2013, **113**, 5364.
5 M. Chhowalla, H. Shin, G. Eda, L. Li, K. Loh and H. Zhang, *Nature Chem.*, 2013, ***5***, *263.*
6 F. Zhou, S. Xin, H. Liang, L. Song and S. Yu, *Angew. Chem. Int. Ed.*, 2014, **53**, 11552.
7 K. Chang and W. Chen, *Chem. Commun.,* 2011, **47**, 4252.
8 P. Wang, H. Sun, Y. Ji, W. Li and X. Wang, *Adv. Mater.*, 2014, **26**, 964.
9 S. Ding, J. Chen and X. Lou, *Chem. Eur. J.*, 2011, **17**, 13142.
10 X. Xie, Z. Ao, D. Su, J. Zhang and G. Wang, *Adv. Funct. Mater.*, 2015, **25**, 1393.
11 J. Ye, L. Ma, W. Chen, Y. Ma, F. Huang, C. Gao and J. Lee, *J. Mater. Chem. A*, 2015, **3**, 6884.
12 X. Cao, Y. Shi, W. Shi, X. Rui, Q. Yan, J. Kong and H. Zhang, *Small*, 2013, **9**, 3433.
13 S. Li, D. Wu, C. Cheng, J. Wang, F. Zhang, Y. Su and X. Feng, *Angew. Chem. Int. Ed.*, 2013, **52**, 12105.
14 J. Yang, D. Voiry, S. Ahn, D. Kang, A. Kim, M. Chhowalla and H. Shin, *Angew. Chem. Int. Ed.*, 2013, 52, 13751.
15 S. Yang, Y. Sun, L. Chen, Y. Hernandez, X. Feng and K. Mullen, *Sci. Rep.*, 2012, **2**, 427.
16 J. Yan, Z. Fan, T. Wei, W. Qian, M. Zhang and F. Wei, *Carbon*, 2010, **48**, 3825.
17 K. Jasuja and V. Berry, *ACS Nano*, 2009, **3**, 2358.
18 Y. Cho, H. Kim, H. Im, Y. Myung, G. Jung, C. Lee, J. Park, M. Park, J. Cho and H. Kang, *J. Phys. Chem. C*, 2011, **115**, 9451.
19 F. Zou, X. Hu, Z. Li, L. Qie, C. Hu, R. Zeng, Y. Jiang and Y. Huang, *Adv. Mater.*, 2014, **26**, 6622.
20 Z. Zhang, G. Li, H. Peng and K. Chen, J. *Mater. Chem. A*, 2013, **1**, 15429.
21 H. Wang, H. Peng, G. Li and K. Chen, *Chem. Eng. J.*, 2015, **275**,160.
22 Li. Y, H. Peng, G. Li and K. Chen, *Eur. Polym. J.*, 2012, **48**, 1406.
23 W.S. Hummers Jr and R.E. Offeman, *J. Am. Chem. Soc.*, 1958, **80**, 1339.
24 L. Hu, Y. Ren, H. Yang and Q. Xu, *ACS Appl. Mater. Interfaces*, 2014, **6**, 14644.
25 H. Park, K. Lee, Y. Lee, S. Kim, D. Kim, M. Kim and K. Park, *J. Power Sources*, 2014, **269**, 534.
26 B. Mazumder and A. L. Hector, *J. Mater. Chem.*, 2009, 19, 4673.
27 B. An, S. Xu, L. Li, J. Tao, F. Huang and X. Geng, *J. Mater. Chem. A*, 2013, **1**, 7222.
28 J. Liu, S. Tang, Y. Lu, G. Cai, S. Liang, W. Wang and X. Chen, *Energy Environ. Sci.*, 2013, **6**, 2691.
29 W. Shin, H. Jeong, B. Kim, J. Kang and J. Choi, *Nano Lett.*, 2012, **12**, 2283.
30 L. Tian, X. Wei, Q. Zhuang, C. Jiang, C. Wu, G. Ma, X. Zhao, Z. Zong and S. Sun, *Nanoscale*, 2014, **6**, 6075.
31 U. Sen, P. Johari, S. Basu, C. Nayak and S. Mitra, *Nanoscale*, 2014, **6**, 10243.
32 D. Zhang, Y. Mai, J. Xiang, X. Xia, Y. Qiao and J. Tu, *J. Power Sources*, 2012, **217**, 229.
33 L. Yang, S. Wang , J. Mao, J. Deng, Q. Gao, Y. Tang and O. G. Schmidt, *Adv. Mater.*, 2013, **25**, 1180.
34 X. Xu, Z. Fan, X. Yu, S. Ding, D Yu , and X. Lou, *Adv. Energy Mater.*, 2014, **4**, 1400902.
35 W. Wei, S. Yang, H. Zhou, I. Lieberwirth, X. Feng,and K. Müllen, *Adv. Mater.*, 2013, **25**, 2909.